

# Label-Free Intraoperative Mean-Transition-Time Image Generation Using Statistical Gating and Deep Learning

Yan Shi, *Student Member, IEEE*, Denghui Zhao, Jingyi Yu, Wei Ni, Pengcheng Li, Yun Gu<sup>†</sup>, *Member, IEEE*, Peng Miao<sup>†</sup>, and Shanbao Tong, *Member, IEEE*

**Abstract**—It is of paramount importance to visualize blood dynamics intraoperatively, as this enables the accurate diagnosis of intraoperative conditions and facilitates informed surgical decision-making. Indocyanine green (ICG) fluorescence imaging represents the gold standard for the assessment of blood flow and the identification of vascular structures. However, it has several disadvantages, including time-consuming data acquisition, mandatory waiting periods, potential allergic reactions, and complex operations. Laser speckle contrast imaging (LSCI) provides an alternative for label-free assessment of blood flow; however, it lacks the necessary information for distinguishing arteries from veins and determining blood flow direction. Such information may be inferred from a Mean Transition Time (MTT) image derived from fluorescence imaging. In order to address these challenges, we propose the implementation of a Mixed Attention Dense UNet (MA-DenseUNet), which will be used to generate synthetic MTT images based on statistically gated deep tissue contrast and white light images. The proposed method provides clear delineation of vasculature, differentiation of arteries and veins, decoding of blood flow direction, and a reduction in imaging time by a minimum of 97.69%. This study demonstrates the potential of deep learning to optimize intraoperative optical imaging techniques, thereby providing faster and more efficient label-free surgical guidance.\*

**Index Terms**—Deep learning, Statistical gating, ICG fluorescent imaging, Mean-transition-time, Laser speckle contrast imaging

## I. INTRODUCTION

Vascular imaging plays a crucial role in modern surgical procedures, providing essential information for surgical planning, intraoperative decisions, and postoperative

evaluation[1, 2]. In specialties like neurosurgery[3], cardiovascular surgery[4], and organ transplantation[5], precise visualization of blood vessels is vital to reducing risks and enhancing patient outcomes. Traditional imaging modalities, including indocyanine green (ICG) fluorescence imaging[6], Doppler ultrasound[7], and magnetic resonance angiography[8], have been instrumental in advancing surgical precision. Among them, ICG fluorescence imaging (see Fig. 1 *fluorescence-based method*) is widely regarded as the gold standard for visualizing blood dynamics referred to the dynamic video and the calculated parameters images [9-11], where mean transition time (MTT) image is critical for visualizing blood flow, identifying arteries and veins, and evaluating anastomoses [12, 13].

However, the fluorescence-based method is not without limitations. The use of contrast agents carries the risk of allergic reactions and contraindications in patients with specific conditions [6, 9, 14]. Furthermore, the utilization of contrast agents can extend the duration of surgical procedures due to the time necessitated for their administration and imaging [11, 15, 16]. Furthermore, operational constraints, such as the necessity for specialized equipment and limited depth penetration, further restrict the utility of these techniques in real-time surgical environments.

Label-free optical imaging [17-20] and deep learning [21] offer promising alternatives to overcome these challenges. Laser speckle contrast imaging (LSCI) is a non-invasive technique that enables the visualization of blood flow through the analysis of speckle patterns generated by coherent light interacting with moving red blood cells [22, 23]. Although LSCI offers real-time imaging capabilities, it is unable to differentiate between arteries and veins or to accurately depict blood flow direction. White Light Imaging (WLI), a technique commonly employed for general visualization during surgical procedures, lacks the capacity to provide functional information about vascular dynamics.

\* This work was supported by the Fundamental Research Funds for the Central Universities (YG2023QNA27). (*Corresponding authors*<sup>†</sup>: Yun Gu, Peng Miao).

This work involved animals in its research. Approval of all ethical and experimental procedures and protocols was granted by the Institutional Animal Care and Use Committee (IACUC) of Shanghai Jiao Tong University (No. A2023085).

Yan Shi, Denghui Zhao, Jingyi Yu, Peng Miao, Shanbao Tong are with School of Biomedical Engineering, Shanghai Jiao Tong University, 800 Dongchuan Road, 200240, Shanghai, China (e-mail: pengmiao@sjtu.edu.cn).

Wei Ni is with the Department of Neurosurgery, Huashan Hospital, Fudan University, 12 Middle Wulumuqi Road, 200040, Shanghai, China.

Pengcheng Li is with School of Biomedical Engineering, Hainan University, 58 Renmin Avenue, 570228, Hainan, China.

Yun Gu is with the Institute of Medical Robotics, Shanghai Jiao Tong University, 800 Dongchuan Road, 200240, Shanghai, China (e-mail: yungu@ieee.org).

The supplementary material is included in the attached *Supplementary* file. Source codes and data examples are available at <https://github.com/MPAPS2019/GenerativeMTT>.

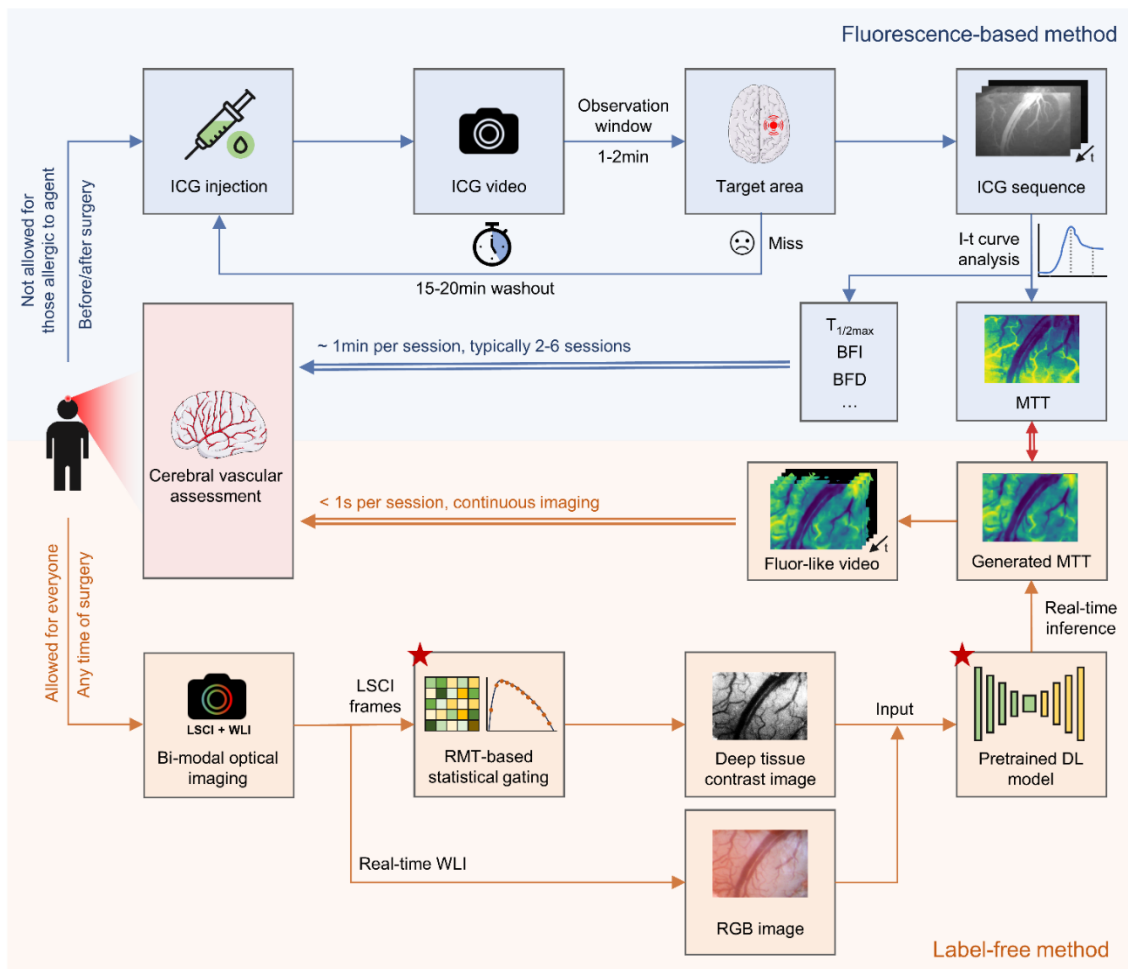


**Fig. 1.** Introduction of the traditional fluorescence-based method and our label-free method for cerebral vascular assessment in neurosurgery. ICG fluorescence imaging is crucial for visualizing blood flow, identifying arteries and veins, and assessing anastomoses during surgery. However, it faces agent-related challenges and significant time constraints, including lengthy data acquisition and waiting periods between imaging sessions. This study proposes a deep-learning-based method using the Mixed Attention Dense UNet (MA-DenseUNet) model to generate synthetic MTT images. This approach overcomes the limitations of original label-free methods and significantly optimizes time efficiency. By applying statistical gating to the multiple scattering component in LSCI, the MA-DenseUNet model effectively resolves depth mismatches across modalities, allowing for more accurate training. The proposed method enhances intraoperative guidance by providing precise vessel type and flow direction information, eliminating the need for fluorescent dyes and substantially reducing the time required for imaging, thus streamlining the surgical process.

The advent of deep learning has transformed the field of medical imaging, enabling the extraction of meaningful patterns from complex datasets. In particular, Convolutional Neural Networks (CNNs) have demonstrated remarkable proficiency in image segmentation, classification, and generation tasks [24]. The integration of deep learning with optical imaging modalities offers the potential for the development of real-time, label-free imaging solutions that provide functional vascular information without the need for contrast agents. Nevertheless, the generation of synthetic MTT images presents a significant challenge, particularly in regard to the depth discrepancy between ICG fluorescence imaging and label-free imaging modalities.

Both ICG fluorescence imaging and label-free modalities (LSCI and WLI) detect backscattered light from tissues [25]. However, there is a discrepancy in imaging depth due to the one-way (ICG fluorescence imaging) or round-trip (LSCI and WLI) paths. ICG fluorescence, which emits incoherent light in a one-way propagation path, has the capacity to penetrate deeper into tissue [26]. In contrast, LSCI and WLI employ light

propagating in round-trip paths, resulting in shallower imaging depths [27]. To address this depth mismatch, we employed a statistical gating method based on a random matrix description. Statistical gating is a sophisticated approach for separating single and multiple scattering components, representing shallow and deep tissues. This method has previously been applied to LSCI [27-29] and visible-light OCT [30], and we adapted it here to isolate the deeper tissue contrast image in LSCI [28], thereby enhancing the structural feature similarities with ICG fluorescence imaging.

This study introduces a novel deep learning framework, the Mixed Attention Dense UNet (MA-DenseUNet), designed to generate synthetic MTT images from deeper tissue contrast image and WLI data. The MA-DenseUNet employs the strengths of DenseNet architectures [31] and attention mechanisms [32] to capture both local and global context. The generated MTT images accurately represent vascular structures, enabling differentiation between arteries and veins and indicating blood flow direction with high accuracy.

In this study, we present a deep learning-based approach to enhance intraoperative blood flow visualization in a label-free, real-time manner (Fig. 1 *label-free method*), validated through experiments on rat models. The primary contributions of this study are as follows:

- **MA-DenseUNet for cross-modality synthesis:** We introduce MA-DenseUNet, a novel network that synthesizes MTT images from LSCI and WLI data without the use of contrast agents, enabling clear visualization of blood flow dynamics, including artery-vein differentiation and blood flow direction.
- **Enhanced imaging depth with statistical gating:** To address the depth discrepancy across source and target modalities, we incorporate a statistical gating technique that selectively isolates the multiple scattering component in LSCI, enhancing deep tissue visibility crucial for accurate blood flow assessment.
- **Real-time intraoperative imaging capability:** Our method achieves a 97.69% reduction in imaging time compared to traditional fluorescence-based techniques, supporting real-time applications and efficient intraoperative decision-making.

## II. MATERIALS AND METHODS

### A. Data acquisition

#### 1) Animal preparations

The animal experiment protocol was approved by the Institutional Animal Care and Use Committee (IACUC) of Shanghai Jiao Tong University (No. A2023085) on July 15, 2023. Imaging data were acquired from adult male Sprague-Dawley (SD) rats ( $n = 23$ ), aged 4~6 weeks and weighing 250~350g. The rats were initially anesthetized with 5% isoflurane for three minutes, and anesthesia depth was monitored through tail and toe pinch reflexes. Once under deep anesthesia, each rat was secured on a stereotaxic frame to maintain head stability. Anesthesia was maintained at 2% isoflurane during surgery. After shaving the head, a central scalp incision exposed the skull, where two cranial windows (1 mm radius) on both hemispheres were created 1 mm posterior to the Bregma. Skull thinning and removal were performed using a dental drill with saline added every 15 seconds to prevent thermal damage. Finally, ICG dye (25 mg dissolved in 50 mL saline) was injected at a dosage of 2 ml/kg via the tail vein.

#### 2) Imaging equipment and settings

All imaging was performed with a modified surgical microscope. The schematic diagram and photograph of the system are illustrated in Fig. 2(a) and Fig. S1, respectively. The system integrates a 3-CMOS camera (FS-3200T-10GE-NNC, Jai, Japan) using three Sony Pregius IMX252 CMOS sensors (1/1.8 inch, 2048×1536 pixels) for capturing three spectral bands (visible 400 ~ 670 nm, NIR1 700 ~ 800 nm, NIR2 820 ~ 1000 nm). The white-light imaging outputs the color images with RGB channels. The monochromatic NIR1 sensor is used for the LSCI, while the NIR2 sensor is used for ICG fluorescence imaging. Illumination was provided by a multi-modality light source, combining a white-light LED (5500K, 2100 lm, EndoView Inc., China) and a 785 nm diode laser

(Thorlabs, USA) via a fiber bundle. The microscope's magnification was set to 2.5× to cover the entire brain.

#### 3) Data acquisition protocol

The data acquisition workflow is depicted in Fig. 2(b). The white light images and raw speckle images (LSCI) were acquired through the white light sensor (15 ms exposure) and NIR1 sensor (5 ms exposure), respectively, at 60 fps over a 3-second period. Auto-white-balance was applied to correct the chromatic aberration in white light imaging. ICG fluorescence imaging was then performed. For ICG fluorescence imaging, a 785 nm laser excited the injected ICG, and fluorescence images were recorded by the NIR2 sensor with a 15 ms exposure at 50 fps, using 16× gain to enhance sensitivity.

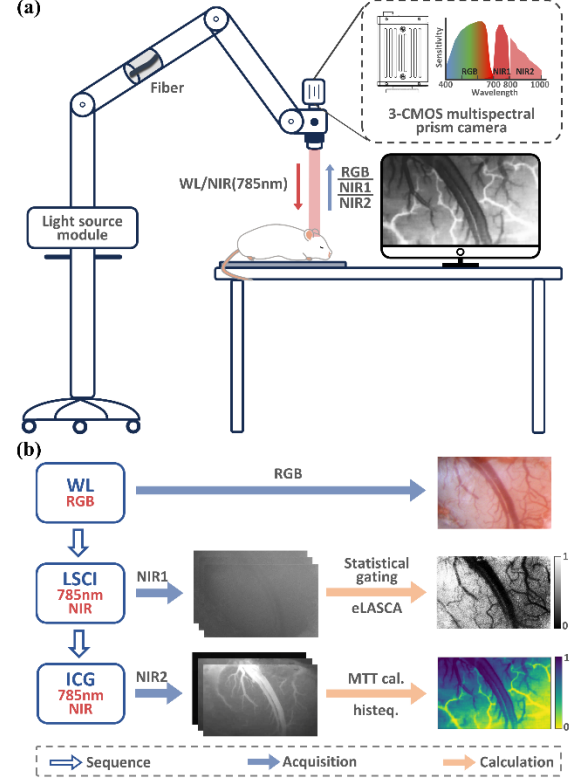


Fig. 2. Experimental setup and workflow for data acquisition and processing in animal experiments. (a) A modified surgical microscope with a multi-modality light source and a 3-CMOS camera was used for image recording. (b) The data acquisition and processing workflow includes white light imaging, laser speckle contrast imaging (LSCI), and ICG fluorescence imaging.

### B. Statistical Gating and Data Processing

To address the depth mismatch between LSCI and ICG fluorescence imaging, we aim to leverage the multiple scattering component in LSCI. In surgical microscope setups, the reflective imaging geometry often obscures multiple scattering components as well as surface reflections and single scattering components. Under coherent light illumination, biological tissue exhibits time-varying speckle patterns, a well-documented phenomenon. In biological tissue, the decorrelation time ( $\tau_c$ ) differs markedly between single and multiple scattering components. The single scattering component, with a significantly longer decorrelation time ( $\tau_{cS}$ ), can reach tens to hundreds of milliseconds [33], while the multiple scattering component ( $\tau_{cM}$ ) typically decorrelates

within less than one millisecond [34]. This distinct difference in decorrelation times enables statistical gating to isolate the multiple scattering component [27].

In practice, we can control the overall recording time  $T$  satisfying  $\tau_{cM} \ll T < \tau_{cS}$  with inter-frame time interval  $\delta T > \tau_{cM}$ . Suppose  $N$  images are recorded during  $T$ , and the pixel size matches the speckle size. For each spatial window ( $M \times M$  pixels) in the speckle image, the intensity values are independent samplings of the speckle intensity distribution. This two-dimensional matrix is flattened into a single-column vector  $I$ . It contains the surface reflection term  $I_R$ , single scattering component ( $I_S$ ), multiple scattering ( $I_M$ ), and interference term  $I_C$ :  $I = I_R + I_S + I_M + I_C$ . Based on the random phasor model of speckle formation,  $I_S$  follows the negative exponential distribution. Due to the diffusive propagation,  $I_M$  has asymptotic Gaussian statistics [35]. The  $I_C$  term is usually trivial and can thus be ignored in this study. Given  $N$  images, column vectors are combined to construct a  $M^2 \times N$  spatiotemporal speckle matrix  $\hat{I}$ . The row-wise centralization is performed on  $\hat{I}$  and outputs the matrix  $I$ . The  $I_R$  term and the DC terms in  $I_S$  and  $I_M$  are eliminated after the centralization, and therefore  $I = I_S + I_M$ . With  $T < \tau_{cS}$ , the  $I_S$  component is a low-rank matrix while  $I_M$  has full ranks. The dynamics make the entries in  $I_M$  have asymptotic Gaussian statistics. Meanwhile, each column of  $I_M$  is an independent sampling under  $\delta T > \tau_{cM}$ . Therefore,  $I_M$  contains independent and identically distributed (*i.i.d.*) entries from the asymptotic Gaussian distribution.

The statistical gating strategy proposed in Ref. [28], based on the Wishart random matrix representation (Eq. 1), was applied. Eq.1 is simplified as Eq.2.  $W_M$  is a Wishart random matrix with *i.i.d.* asymptotic Gaussian entries. The eigenvalue distribution follows the Marchenko-Pastur (MP) distribution (Eq.3).

$$\frac{1}{N} \mathbf{I} \mathbf{I}^T = \frac{1}{N} \mathbf{I}_S \mathbf{I}_S^T + \frac{1}{N} \mathbf{I}_M \mathbf{I}_M^T + \frac{1}{N} (\mathbf{I}_S \mathbf{I}_M^T + \mathbf{I}_M \mathbf{I}_S^T) \quad (1)$$

$$\mathbf{W} = \mathbf{W}_S + \mathbf{W}_M + \mathbf{W}_C \quad (2)$$

$$\rho(\lambda) = \frac{1}{2\pi\sigma^2} \frac{\sqrt{(\lambda_+ - \lambda)(\lambda - \lambda_-)}}{c\lambda} \quad (3)$$

where  $\lambda_{\pm} = \sigma^2(1 \pm \sqrt{c})^2$  are hard bounds.  $\sigma^2$  is the variance of multiple scattering component, and  $c = M^2/N \in (0 \sim 1)$ .

Given that  $I_S$  is low-rank, both  $W_S$  and  $W_C$  are thus low-rank. Therefore,  $W$  is a low-rank perturbation of Wishart random matrix (RM). The perturbations ( $W_S$  and  $W_C$ ) result in eigenvalues out of support of MP distribution, i.e.,  $\lambda > \lambda_+$  or affects the larger eigenvalues in MP distribution. We use the minimal eigenvalue of  $W$  to estimate  $\lambda_-$  in the MP distribution of  $I_M$ . Then, the  $\sigma^2$  can be obtained. Due to  $I = I_S + I_M$ , the variance of  $I_S$ , i.e.  $\sigma_S^2$ , is estimated by  $\sigma_S^2 = \sigma_H^2 - \sigma^2$ . Here,  $\sigma_H^2$  is the variance of entries in the averaged column vector from  $I$ . Since the single scattering component follows a negative exponential distribution, the first-order moment (ensemble average) is obtained by  $\mu_S = \sigma_S$ . After that, the first-order moment of multiple scattering component is retrieved by  $\mu_M = \mu_H - \mu_S - \mu_R$ . Here,  $\mu_H$  is the mean value of entries in the averaged column vector of  $I$ .  $\mu_R$  is the surface reflection part estimated by the Monte Carlo simulation (*Supplementary S1*).

In accordance with the principles of LSCI, the first and second-order statistics of  $I_M$  are used to retrieve the deep tissue

contrast image (Eq.4). The relation between contrast value  $K$  and blood flow velocity  $v$  is proportional to  $1/K^2$ . In this study, the deep tissue contrast image participates in deep learning.

$$K = \frac{\sigma_M}{\mu_M} \quad (4)$$

The MTT image was calculated from the ICG fluorescence imaging sequence. The calculation is pixel-wised based on the time-dependent intensity signal  $I(t)$  (Eq.5). Mathematically, the MTT value represents the center of mass of the intensity curve, encompassing the period from the onset of ICG until the signal stabilizes.

$$MTT = \frac{\sum_t t \cdot I(t)}{\sum_t I(t)} \quad (5)$$

### C. MA-DenseUNet architecture

The proposed Mixed Attention Dense UNet (MA-DenseUNet) is an enhanced UNet variant, as shown in Fig. 3(a). Its input is a 4-channel patch of size  $4 \times 256 \times 256$ , formed by concatenating the white light and deep tissue contrast images. This input patch passes through a convolutional layer ( $k=3, s=1, p=1$ ) and an activated batch normalization (ABN) layer and transformed into a 16-channel feature map ( $16 \times 256 \times 256$ ). ABN layer performs the batch normalization and uses the ReLU activation function (see Fig. 3(b-ii)) [36].

The encoding process includes four steps, each with a dense module, a transition layer, and a mixed attention (MA) module, doubling the channels and halving the spatial dimensions at each stage. The dense module (Fig. 3(b-i)) promotes feature reuse and reduces overfitting, yielding better performance with fewer parameters [31]. It has two layers, each (Fig. 3(b-ii)) generates a  $C/2$ -channel feature map ( $C$  is the number of input channels), and connects layers by concatenating feature maps from previous steps. A transition layer with an ABN layer and a convolutional layer down-samples the output.

The mixed attention module (Fig. 3(c-i)) sequentially combines channel and spatial attention mechanisms to learn what and where to be emphasized [32]. Given the input feature map  $F_{in} \in \mathbb{R}^{C \times H \times W}$ , the channel attention (CA) submodule (Fig. 3(c-ii)) produces the channel attention map  $AW_C \in \mathbb{R}^{C \times 1 \times 1}$  by applying average and max pooling spatially, followed by a shared multi-layer perceptron MLP and sigmoid activation. The output  $F_{CA} = \mathbf{CA}(F_{in}) \otimes F_{in}$  is then processed by the spatial attention (SA) submodule (Fig. 3(c-iii)), producing a spatial attention map  $AW_S \in \mathbb{R}^{1 \times H \times W}$ . SA applies pooling across channels, followed by a convolutional layer ( $k=7, s=1, p=3$ ) and a sigmoid function. The final output feature map  $F_{out}$  is calculated as  $F_{out} = \mathbf{SA}(F_{CA}) \otimes F_{CA}$ , where  $\otimes$  denotes element-wise multiplication with broadcasting.

Decoding occurs in four steps, each with a dense block, up-sampling (via transpose convolution), a transition layer, and an attention block, halving the channels and doubling the spatial size at each stage. Skip connections link corresponding layers in the encoder and decoder to enhance feature fusion. Deep supervision along the decoder refines feature representation and accelerates convergence [37], while up-sampling ensures calculation for the weighted loss function  $L_{total}$ . The final convolutional layer which outputs a single-channel MTT image ( $1 \times 256 \times 256$ ).

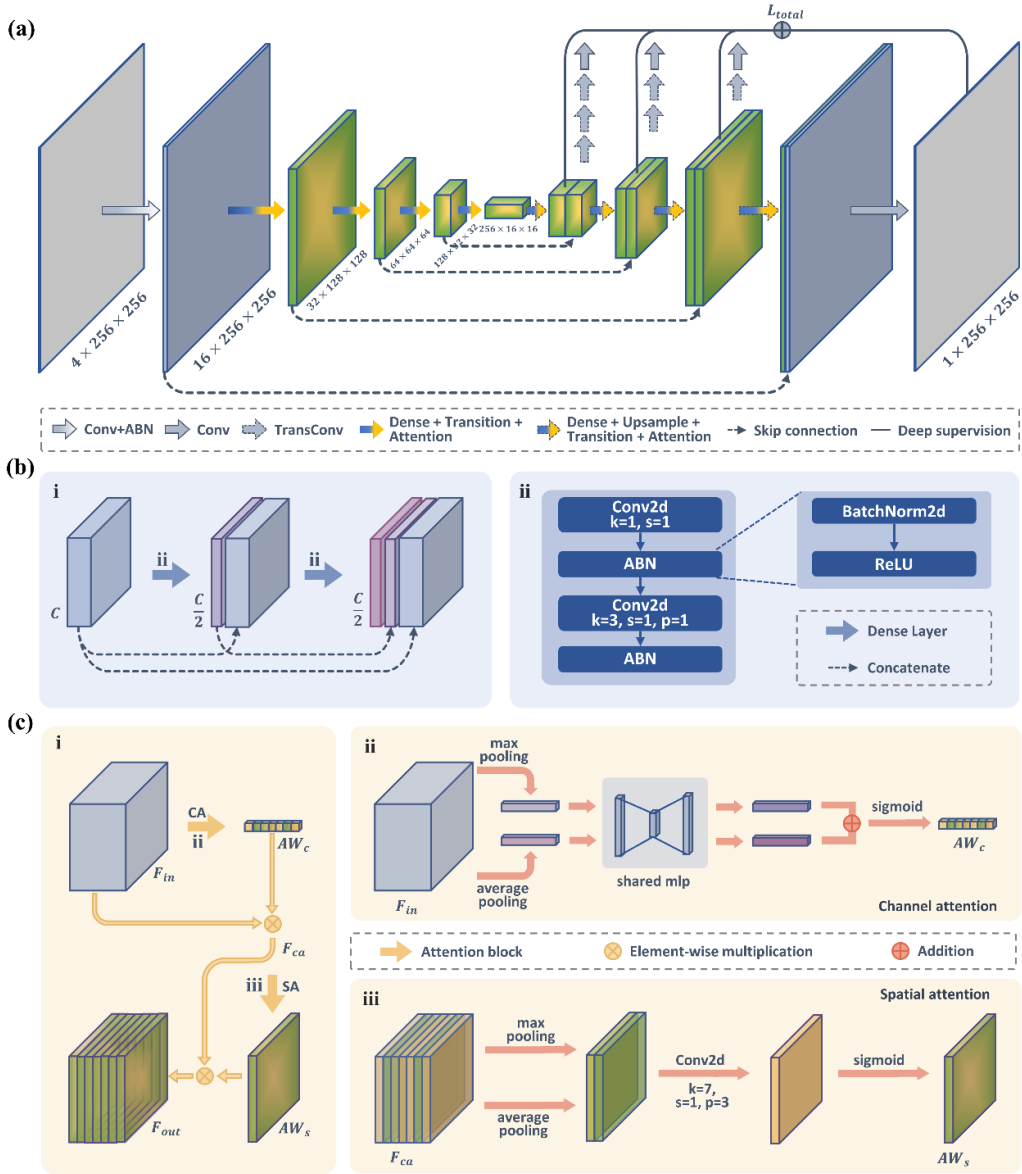


Fig. 3. Overview of the proposed MA-DenseUNet architecture. (a) The overall structure of MA-DenseUNet, incorporating dense blocks and mixed attention (MA) modules in each layer. (b) Detailed breakdown of the dense block, showing its architecture (i) and operational sequence (ii). (c) Breakdown of the mixed attention module (i), which integrates a channel attention module (ii) and a spatial attention module (iii).

## D. Training and evaluation

### 1) Training dataset

The training dataset includes four-channel images that combine the three channels from the white-light image, and one from the deep tissue contrast image. This contrast image is calculated from 30 frames of speckle images (Eq. 4), while the MTT image derived from the ICG fluorescence imaging sequence serves as the ground truth (Eq.5). To address scale differences across the white-light, contrast, and MTT images, normalization is performed. Afterwards, registration between three modality images is performed using a 2D cross-correlation metric[38]. Regions of interest (ROIs) covering the cranial window were selected from each pair of data.

The dataset comprises 46 samples collected from rat brain hemispheres. Of these, five are excluded due to preparation issues, and ten others are designated as the *Test\_Poor* dataset due to poor ICG perfusion in the ground truth MTT image,

despite qualified input images (see Fig. 5, labeled *Test\_Poor1* and *Test\_Poor2*). The remaining 31 samples are randomly split by rat into a training dataset (25 samples from 15 rats) and a test dataset (the *Test\_Normal* dataset, 6 samples from 3 rats).

For training, a 10-fold cross-validation method is applied, along with data augmentation to reduce overfitting. During each training epoch, 200 patches were randomly sampled from each data based on various transformations, including random rotation (angle  $\theta_r \in [-10, 10]^\circ$ ), random cropping (side length  $a \in [256, 512]$ ), and random flipping (60% probability). These patches were then all resized to  $256 \times 256$  pixels.

### 2) Loss function

The loss function incorporates vessel sensitivity to optimize image-to-image training for MA-DenseUNet, as follows:

$$L_{total} = \sum_{i=1}^4 \alpha_i \cdot \left( \frac{1}{N} \sum_{j \in \mathcal{P}} (y_j - \hat{y}_{ij})^2 + \frac{1}{M} \sum_{k \in \mathcal{M}_v} (y_k - \hat{y}_{ik})^2 \right) \quad (6)$$

where  $\alpha_i$  represents the weight for each decoder layer, valued at 0.125, 0.125, 0.125, and 0.5, respectively.  $N$  and  $M$  represent the pixel counts for the full patch  $\mathbf{P}$  and the vasculature mask  $\mathbf{M}_v$ , respectively. The pixel value  $y_*$  and  $\hat{y}_{i*}$  correspond to ground truth and prediction for layer  $i$ , with the subscripts  $j$  and  $k$  indexing pixels in  $\mathbf{P}$  and  $\mathbf{M}_v$ , respectively. The vasculature mask is created by adaptive segmentation of the maximum-intensity fluorescence image, followed by manual refinement.

### 3) Evaluation metrics

Both full-reference and no-reference image quality assessments [39] are utilized to evaluate the performance of our MA-DenseUNet model. Full-reference assessments consist of the mean squared error (MSE) for the entire image and vessel-specific regions, as well as the structural similarity index measure (SSIM) for the vessel area. No-reference indicators include contrast-to-noise ratio (CNR, Eq.7) and signal-to-noise ratio (SNR, Eq.8).

$$CNR = 10 \log(|\mu_v - \mu_b|/\sigma_b) \quad (7)$$

$$SNR = 10 \log(\mu_v/\sigma_b) \quad (8)$$

where  $\mu_*$  and  $\sigma_*$  represent the mean value and standard error, with subscripts  $v$  and  $b$  representing vascular and background areas, respectively.

### 4) Implementation details

The model is implemented in PyTorch IDE and trained on an NVIDIA RTX 4070Ti GPU card with 12GB memory. The training and inference are conducted using the open-source platform *Detectron2*, developed by Meta Inc. The AdamW optimizer was employed with parameters  $\beta_1=0.9$ ,  $\beta_2=0.99$ ,  $\lambda=0.01$ . The  $L_2$  regularization is introduced to prevent overfitting. The initial learning rate was set to 0.01 and decreased by a factor of 0.1 at first-, half-, and third-quarter epochs. We conduct 100 epochs in the training procedure. Training spans 100 epochs, with each epoch comprising 200 random samples from the 25 training samples (batch size of 10), resulting in 50,000 iterations.

To assemble the full prediction image, we apply a Gaussian-weighted patch-combining strategy with a 2D Gaussian weight ( $\sigma=0.25$ ) per patch, which helps maintain prediction consistency and reduces boundary artifacts. Each patch, sized  $256 \times 256$  pixels, overlaps with neighboring patches by a stride of 128 along both axes.

### E. Generating ICG fluorescence-like video

The generation of ICG fluorescence-like video is achieved through the utilization of a synthetic MTT image. The MTT image represents vascular perfusion time, where a smaller intensity value indicates an earlier appearance of the fluorescence signal in the ICG video sequence. Thus, the intensity values in the image can be used to convert a 2D image into a time series. In the case of a synthetic MTT image, the intensity value,  $I_{MTT}$ , ranges from 0 to 1. First, it is converted into a 256-bit grayscale image. At this stage, the intensity is a scalar without physical meaning. We need to manually align the start and end times of the grayscale MTT image with the actual time domain based on the original ICG video. By determining the time when the vessels start to light up ( $T_s$ ) and when they are fully illuminated in the original ICG video ( $T_e$ ), we can calculate the frames  $N_f$  within this duration, as  $N_f = fr \times (T_e - T_s)$ , in which  $fr$  is the frame rate ( $fr = 50$  fps in our

experiment). The obtained  $N_f$  is much smaller than 256 (roughly 60-70 frames). By assuming the fluorescence signal in the vessels increases uniformly over time, the frame image at time  $T_s + t$  corresponding to the original ICG video is composed of all pixels in the synthetic MTT image with intensity less than  $t \times [256/N_f]$ :

$$frame_{MTT}(T_s + t) = I_{MTT}(I_{MTT} \leq t \times [256/N_f]). \quad (9)$$

The base image could further be replaced by a deep tissue contrast image for better visualization, as

$$frame_{LSI}(T_s + t) = I_{LSI}(MTT \leq t \times [256/N_f]). \quad (10)$$

## III. RESULTS

### A. Statistical gating of the deep tissue contrast image

The dynamics of biological tissue in vivo result in differences in speckle decorrelation time for the single and multiple scattering components in recorded speckle patterns [34]. The asymptotic Gaussian statistics of the multiple scattering component enable a statistical gating method based on Wishart random matrix representation under coherent light illumination (*Materials and Methods B*) [27]. The deep tissue contrast image can be reconstructed from the gated multiple scattering component, revealing the vasculature and blood flow in deep tissues. Fig. 4d and Fig. 4e shows the rat brain's original and deep tissue contrast images, respectively. Traditional LSCI reveals more superficial blood flow information due to the surface reflection or single scattering component. Deep tissue contrast images compensate for the depth mismatch between the LSCI and ICG fluorescence imaging and lead to better structural similarity with the MTT image (Fig. 4f) calculated from ICG fluorescent imaging (red boxes in Fig. 4d and Fig. 4e). The deep tissue contrast image also enhances structural contrast between vessels and surrounding tissue, as shown in the signal profiles (Fig. 4g) along the white lines in Fig. 4d and Fig. 4e. For all datasets (41 samples involved in training and inference), the contrast noise ratio (CNR) of deep tissue contrast images is  $0.5359 \pm 0.7334$ , better than that of traditional contrast images ( $0.4648 \pm 0.8971$ ).

The imaging depth can be estimated from the path-length distribution of photon trajectories with the Monte Carlo simulation [40, 41] (Supplementary S3). Fig. 4b and Fig. 4c show the single scattering path-length distribution  $\rho_S(s)$  and multiple scattering path-length distribution  $\rho_M(s)$  obtained from the rat's cerebral cortex phantom (Fig. 4a, also see the Supplementary S3). The scattering mean free path  $l_s = 1/\mu_s$  and transport mean free path  $l_t = 1/\mu'_s$  are characteristic parameters in path-length distribution. Both single and multiple scattering parameters in path-length distribution. Both single and multiple scattering path-length fit well with the analytical distribution (Eqs.S1 and S2 in Supplementary S3). The single scattering component in the rat's brain is found to be approximately  $0.20l_s$ , equivalent to 0.012 mm in this simulation. 95% of signals come from the depth between 0 and  $0.61l_s$  ( $[0 \sim 0.036$  mm]). The average penetrating depth of multiple scattering component is  $1.07l_t$  (0.64 mm). The distribution of penetrating depth is peaked at  $3.26l_s$  (approximately 0.20 mm). The 95% of signals around peaks come from the range  $[0.63l_s \sim 3.07l_t]$  ( $[0.038$  mm  $\sim 1.84$  mm]). Regarding light intensity, the multiple scattering

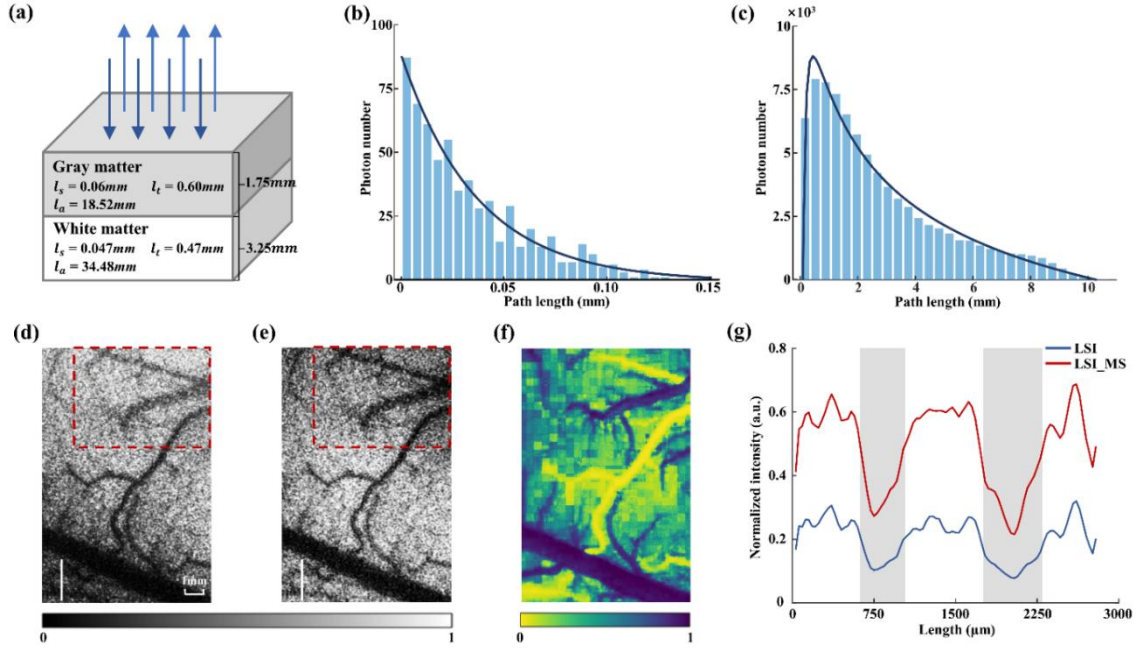


Fig. 4. Monte Carlo simulation and deep tissue contrast image reconstruction. (a) is the Monte Carlo simulation phantom of rat brains. (b) and (c) show the path-length distribution of single and multiple scattering components. (d) and (e) show the traditional and deep tissue contrast images, respectively. (f) is the corresponding MTT image calculated from the ICG fluorescent imaging. (g) plots the contrast data profiles along the white lines in (d) and (e).

component accounts for only 26.06% of the total recorded speckle image. For clinical brain surgery, the human brain gray matter has  $l_s = 0.1 \text{ mm}$  and  $l_t = 1 \text{ mm}$  [42], while the white matter has reduced  $l_s = 0.05 \text{ mm}$  and  $l_t = 0.5 \text{ mm}$  [43]. The multiple scattering component can retrieve up to 3 mm depth for gray matter or 1.5 mm depth for white matter in brain surgery based on the results of Monte Carlo simulation. An ideal detector with 100% quantum efficiency is assumed in the above analysis. In practice, the limited quantum efficiency of the detector decreases the overall penetration depth.

### B. MA-DenseUNet enables MTT mapping for vascular differentiation

The MTT image calculated from ICG fluorescent imaging (Eq. 5) works as the ground truth, facilitating end-to-end training from the white light and deep tissue contrast images acquired from WLI and LSCI, respectively. The MA-DenseUNet model (*Materials and Methods C*) is developed and trained to generate synthetic MTT images. Fig. 5 illustrates four typical examples, including two high-quality and two low-quality examples. The first two columns show the inputs of the white-light images and the deep tissue contrast images. The third column shows the synthetic MTT images. The ground-truth MTT images are shown in the fourth column. Compared to the ground-truth MTT images, the trained MA-DenseUNet works well for the four examples. The arteries and veins in the synthetic MTT images are clearly and correctly generated. The  $L_1$  error between the MA-DenseUNet output and ground truth (the fifth column in Fig. 5) further corroborates the high accuracy in vessel area by MA-DenseUNet model. We could refer to the last column in Fig. 5 for more details.

Regarding artery and vein identification, slight differences in color and size between A1 and V1 could still be observed in the white light image of *Test\_Normal1*. The MTT image, however,

provides a more visual and accurate assessment. Another challenging task in intraoperative applications is determining branching relationships. For example, the origin of the A2 vessel within the white-dotted circles is hardly discernible in the white light image or deep tissue contrast image. Both the ground truth and the synthetic MTT images reveal the branching relationships. The synthetic MTT images are less noisy than the ground truth, primarily due to using mean squared error (MSE) as the loss function during training. The MSE loss assumes Gaussian distribution in the synthetic image, which helps reduce noise in the output.

In contrast, the ground-truth MTT images contain noise introduced by various factors during fluorescence imaging, such as background fluorescence, fluorescence leakage, and motion artifacts. Both CNR and SNR are significantly improved in poor-quality test datasets mainly due to inadequate ICG perfusion (Table 1). Poor perfusion can result in incomplete and blurry vessels (V3 and V4 in Fig. 5) in the ground-truth MTT image. In contrast, these vessels are distinct and complete in the synthetic MTT images. Poor perfusion is a common challenge in intraoperative ICG fluorescence imaging, and the MA-DenseUNet thus provides a robust solution.

TABLE I  
COMPARISON BETWEEN GROUND-TRUTH AND SYNTHETIC MTT IMAGES

Samples	CNR		SNR	
	ground-truth	synthetic	ground-truth	synthetic
Test_Normal1	2.9545	3.6647	5.7936	6.9895
Test_Normal2	1.6707	2.9152	5.3143	6.6688
Test_Poor1	0.7574	3.7027	4.8397	6.8591
Test_Poor2	-0.2069	2.6336	4.2084	6.8473

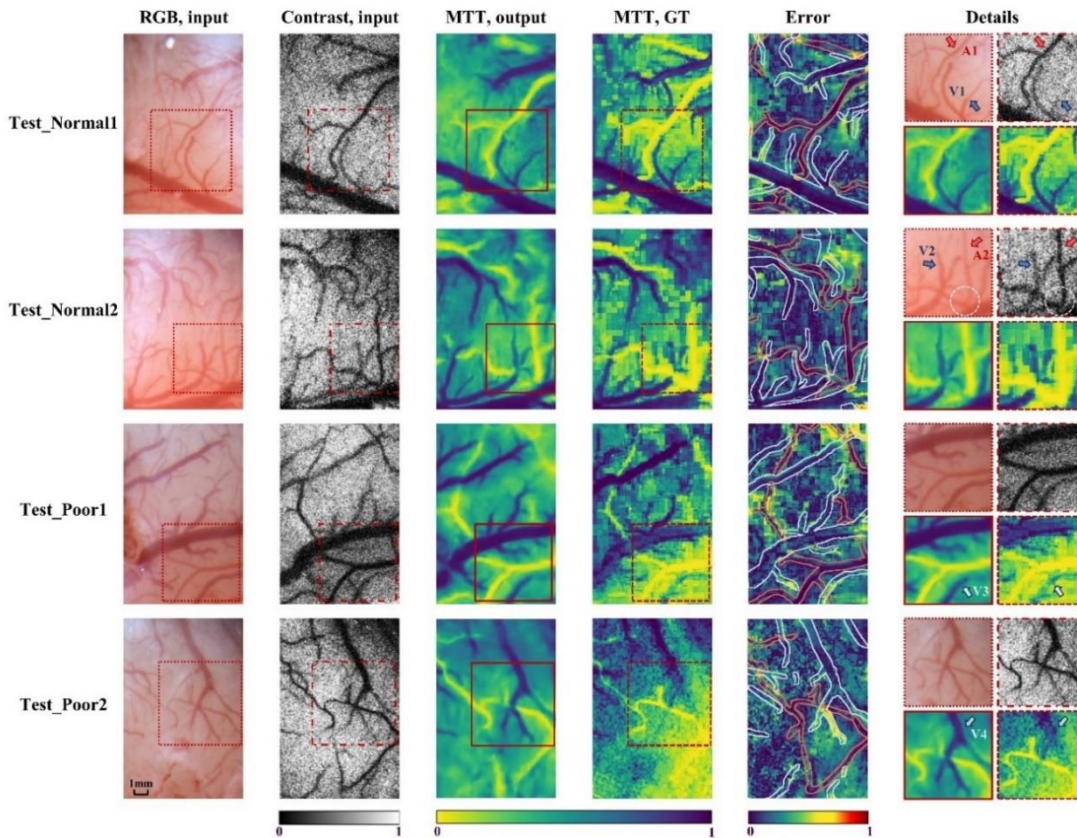


Fig. 5. The synthetic MTT images generated by the MA-DenseUNet model. The first and second columns show the inputs, *i.e.*, white light images and deep tissue contrast images. The synthetic MTT images are shown in the third column. The fourth and fifth columns are the ground-truth MTT and L1 error images, respectively. The last column stitches the red-box ROIs to facilitate the comparison. Four samples (two from the normal test set and two from the poor-quality test set) are shown in different rows. The boundaries of arteries and veins in the L1 error image are marked by red and white lines, respectively.

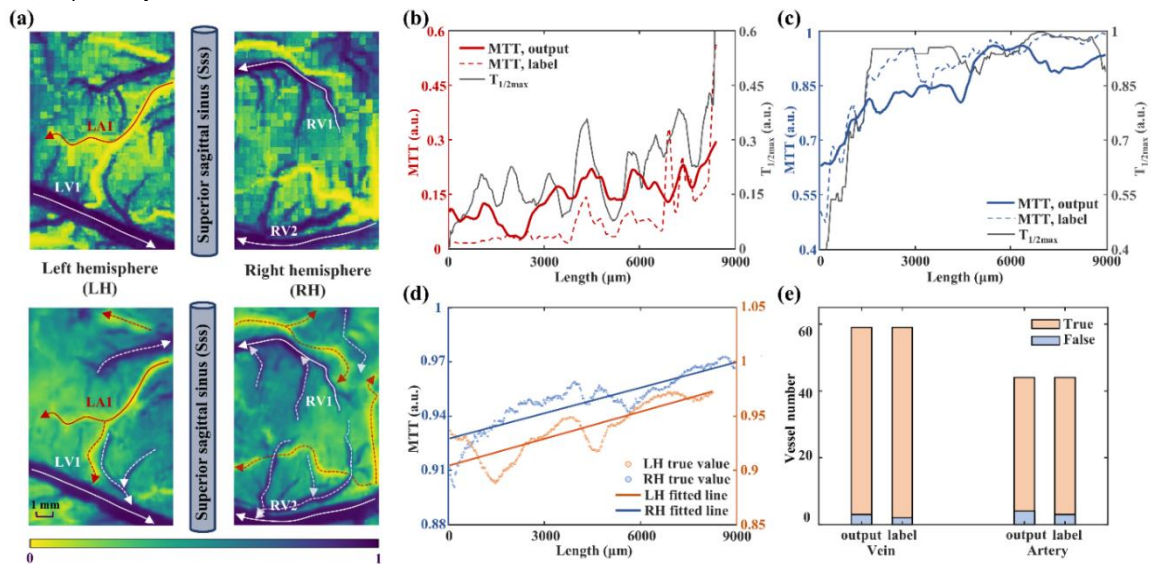


Fig. 6. Determining the blood flow direction from the synthetic MTT images. (a) synthetic MTT images (bottom row) and their ground truth (top row) were obtained from one rat's cerebral hemispheres. All arrow lines with labels on the vessels indicate the direction of blood flow. (b) and (c) display the synthetic and ground-truth MTT values and  $T_{1/2max}$  values along LA1 and RV1, illustrating blood flow direction from low to high values.  $T_{1/2max}$  is another indicator of blood flow direction [44]. (d) is the synthetic MTT values along LV1 and RV2, with their corresponding fitted lines, demonstrating two vessels in the left and right hemispheres drained into the superior sagittal sinus. (e) the vessel numbers with correct and incorrect detection of flow directions based on the synthetic MTT images and  $T_{1/2max}$  images.

### C. Decoding flow direction from synthetic MTT image

Determining the direction of blood flow is critical during surgery, as it assists surgeons in identifying upstream and

downstream blood flows and detecting any malfunctioning vessels. For example, surgeons need to occlude the upstream vessel promptly in the event of bleeding downstream, facilitating

timely hemostasis, which could be more efficient if the blood flow direction is known. In ICG fluorescence imaging, the direction of blood flow is identified by directly analyzing a fluorescence video. The blood flow direction can also be determined from the  $T_{1/2max}$  or MTT images [44].  $T_{1/2max}$  is the time for the fluorescent brightness to rise from baseline to half of the peak intensity. In a single vessel, lower  $T_{1/2max}$  or MTT values implies faster ICG flow, but higher values indicate a slow ICG flow. Here, we find that the synthetic MTT images demonstrate comparable performance in decoding the direction of blood flow.

Fig. 6(a) shows the synthetic MTT images (bottom row) and their corresponding ground truth (top row) from both hemispheres of a rat. According to the anatomy of brain vasculature, the superior sagittal sinus (Sss), located within the superior margin of the falx cerebri, collects blood from the cerebral hemispheres. Fig. 6(b) and Fig. 6(c) show the profiles of MTT and  $T_{1/2max}$  values along the vessel LA1 and RV1 denoted by arrows in both synthetic and ground-truth MTT images. According to the trends of MTT and  $T_{1/2max}$  signals, we can thus infer arteries when the blood flows from the main vessel to the branches, but veins if the blood flow in the opposite direction, which complies with the circulation anatomy as well.

Additionally, the two largest veins in each hemisphere, namely LV1 and RV2, which are branches of the Sss, are also compared. The MTT value profiles and the corresponding linear fitting results along the two veins (indicated by arrows in Fig. 6(a)) are plotted in Fig. 6(d). These profiles illustrate blood drainage from each hemisphere into the Sss, consistent with anatomical expectations. Furthermore, slope of the linear fitting is a robust indicator for blood flow determination. A positive slope indicates that blood flows from the start of the line toward its end, and vice versa for a negative slope. Using the  $T_{1/2max}$  image as a reference, we summarized the accuracy of slope indicator in both the synthetic and ground-truth MTT images, including totally 59 veins and 44 arteries in the test set, as shown in Fig. 6(e). The detection of blood flow direction in synthetic MTT images achieves an accuracy of 94.92% for veins and 90.91% for arteries, respectively. The dashed lines with arrows in Fig. 6(a) show the blood flow directions determined by the synthetic MTT.

Moreover, during an intraoperative procedure, physicians often rely on visually observing ICG fluorescence videos to manually estimate blood flow velocity and direction, a practice that can be both subjective and time-consuming. To further shorten the learning curve and enhance usability, we generate an ICG fluorescence-like video from the synthetic MTT map and deep tissue contrast image (*Materials and Methods E*). Fig. S2 presents the key-frames from the synthetic ICG fluorescence-like video and the corresponding ground-truth ICG video (also see Video S1 for details).

#### D. MA-DenseUNet accelerate intraoperative vascular imaging

Cross-modality generation offers a unique computational approach for wide-field intraoperative imaging of biological tissues, effectively expediting vascular visualization in clinical settings. Unlike traditional ICG fluorescence imaging, which demands extensive preparation and a minimum 40-second acquisition window post-ICG administration, our deep-

learning-based method requires only 1/50 s to capture continuous white light and laser speckle images, followed by an initial 0.6 s computation for the first contrast image. Using a sliding window strategy, this method continuously generates synthetic MTT images, eliminating the need for the typical 15-minute interval between consecutive ICG injections.

On the same GPU platform, generating one MTT image at 1024×1024 resolution from an ICG video takes 16.38 s, while the MA-DenseUNet model achieves the same in only 0.70 s. This offline assessment highlights that, by considering both imaging and processing, our approach reduces time expenditure by at least 97.69% compared to conventional fluorescence imaging (from 56.38 s down to 1.3 s), even disregarding inter-session waiting times. In arteriovenous malformation (AVM) surgeries, which typically involve 2-4 imaging sessions [45], this time efficiency translates to a potential reduction of 17-50 minutes. Video S2 demonstrates the method's real-time capability for generating MTT images in situ.

## IV. DISCUSSION

### A. Mechanism in cross-modality generation

We demonstrated that MA-DenseUNet could generate synthetic MTT images from white light and deep tissue contrast images—the modality transformation from label-free to fluorescence roots in their structural similarities. Fig. 7(b) shows the signal profile along the white line in Fig. 7(a) (sample *Test\_Normal1*), crossing a vein (V1) and an artery (A1). The luminance derived from the RGB channels is used in data profiling of white light images. The vessel diameters are determined by measuring the full width at half prominence (FWHP) values across all image modalities.

Although all three modalities present similarities in vasculature structure, the white light image outputs a narrower vein V1 (596.9  $\mu\text{m}$ ) than that by either deep tissue contrast image (677.1  $\mu\text{m}$ ) or ground-truth MTT image (720.1  $\mu\text{m}$ ). The main reason is that the penetration depth of visible light is significantly shallower than infrared light's. The vasculature networks in the deep tissue contrast image and ground-truth MTT image are highly similar, in line with their similar penetration depths. However, the propagation of incoherent fluorescence light leads to blurred vessel boundaries and, thus, larger vessel diameter in the ground-truth MTT image than the deep tissue contrast image. The modality transfer, however, could successfully recover the structure features in the synthetic MTT image, e.g., V1 with a diameter of 673.2  $\mu\text{m}$ .

Similarly, such a proportional relationship in vessel diameter from different modalities is also found in arteries. For artery A1, the white-light modality outputs a minimum vessel diameter (422.1  $\mu\text{m}$ ). The ground-truth MTT image provides an estimate of 968.2  $\mu\text{m}$ , compared with that from the deep tissue contrast image (694.5  $\mu\text{m}$ ), which is close to that by the proposed MA-DenseUNet and synthetic MTT images (749.1  $\mu\text{m}$ ). We believe the MA-DenseUNet can be applied to other imaging modality transfer tasks based on their feature similarity.

### B. Attention mechanism in training

The attention mechanism is the key to training of the proposed MA-DenseUNet. To evaluate the mixed attention module's performance, we obtain the attention weights of

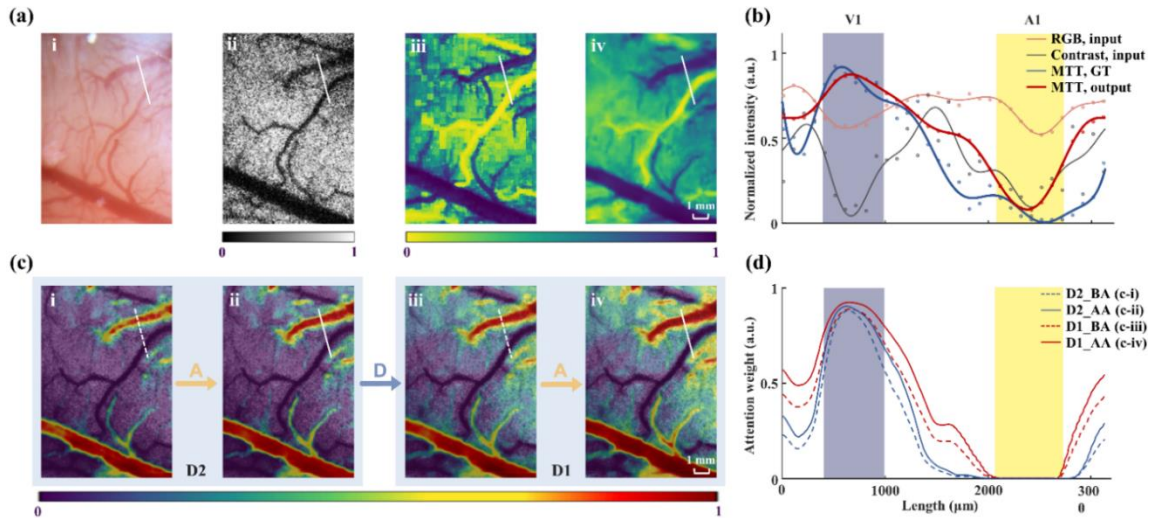


**Fig. 7.** Morphological analysis of vasculature in different modalities, with Grad-CAM outputs from the mixed attention module in the last two decoder layers. (a) displays the white light image (i), deep tissue contrast image (ii), ground-truth MTT image (iii), and synthetic MTT image (iv). The graphs representing the normalized data profiles along the white lines in (a) are presented in (b). The cross-sections of the vein V1 and the artery A1 are highlighted in gray and yellow, respectively. (c) shows the attention maps superimposed on the deep tissue contrast images (a-ii), demonstrating the attention weights before and after the attention module in the last two decoder layers. The arrow denotes the decoder path, where *A* and *D* represent the mixed attention module and the dense block, respectively. Attention weight profiles along the white dashed lines in (c) are plotted in (d), demonstrating attention enhancement in both arteries and veins.

feature maps in the last two decoder layers using Grad-CAM (Gradient-weighted Class Activation Mapping). Grad-CAM provides visual explanations for the MA-DenseUNet model by weighting the multi-channels of the feature map based on the gradient. Fig. 7(c) shows the feature maps superimposed on the deep tissue contrast images. The arrows in Fig. 7(c) indicate the deep tissue decoding pipeline from decoder layer 2 (D2) to decoder layer 1 (D1), with *A* and *D* representing the attention and dense block modules, respectively. We can see the distinct attention weights in the tissue areas by comparing the input-output attention maps across modules (Fig. 7(c)). The weights of arteries and veins cluster at two opposite ends, respectively. The profiles of attention weight along the white lines are plotted in Fig. 7(d).

Peak analysis evaluates attention maps across modules (method in *Supplementary S3*). Table S1 summarizes the measures for both V1 and A1 in different modules, including peak value, width at half prominence, and peak-width ratio (PWR). Along the decoding pipeline, the attention width of A1 and V1 asymptotically approaches the vessel diameters  $\omega_0$ . Comparing attention maps before and after the attention module (D2\_BA vs. D2\_AA, and D1\_BA vs. D1\_AA), we can see that the MA-DenseUNet gives more concentration in attention on both arteries and veins and distinct contrast between vessels and tissues, as indicated by the increased PWR for both V1 and A1. We also compare our MA-DenseUNet with three potential models: UNet, Dense-UNet with deep supervision, and MA-DenseUNet, where UNet serves as the baseline (Fig. S3). Table S2 summarizes both full-reference indicators (MSE, vMSE, and vSSIM) and no-reference indicators (CNR and SNR) for each model. The MA-DenseUNet with deep supervision outperforms other UNet-based models, which attests to the efficiency of dense and mixed-attention blocks and the deep supervision strategy.

### C. Clinical implications

Our method represents a significant advancement in intraoperative imaging by providing detailed vascular

information—artery-vein differentiation and blood flow direction—without the need for contrast agents like ICG. Although effective, traditional ICG fluorescence imaging is limited by lengthy acquisition times, required waiting periods, and risks associated with repeated dye administration, including potential allergic reactions. By synthesizing MTT images using LSCI and WLI, our approach achieves a nearly 98% reduction in imaging time and avoids the need for invasive agents.

The MA-DenseUNet model’s ability to generate synthetic MTT images that closely match ICG-based images marks a breakthrough in non-invasive intraoperative imaging. Its strong performance, demonstrated by improved structural similarity metrics, highlights its potential for broader clinical use. This rapid provision of vascular information could enhance surgical decision-making, improving outcomes while reducing operating room (OR) time.

Beyond vascular neurosurgery, our cross-modality generation framework could transform other surgeries requiring rapid blood flow assessment, such as cardiovascular procedures and organ transplantation. By enabling continuous, label-free imaging, it reduces time in OR and eliminates contrast-related risks, promoting safety. Furthermore, this approach could be adapted to other imaging modalities, such as hyperspectral imaging or optical coherence tomography (OCT), enhancing its versatility and broadening its clinical applications.

### D. Limitations and future work

While our results are promising, there are several limitations to consider. First, the reliance on LSCI and WLI, while providing valuable structural and perfusion information, may not meet the depth requirements of complex surgical environments with intricate vascular networks. Future work could explore integrating additional label-free modalities, such as near-infrared spectroscopy (NIRS) or OCT, to enhance depth resolution and vascular mapping.

Extensive clinical validation is necessary. Although effective

in animal studies, further trials on human subjects are needed to assess the model's robustness in real surgical environments. A larger dataset encompassing diverse vascular structures and pathologies would further improve accuracy and generalizability.

Additionally, the MA-DenseUNet model's use of mean squared error (MSE) as a loss function introduces a slight smoothing effect, which, while reducing noise, may obscure fine vascular details in some cases. Future research could incorporate advanced loss functions, like perceptual or adversarial loss, to preserve small vessel structures while maintaining robustness.

Looking ahead, there are several exciting directions for future research. One is real-time generation of fluorescence-like videos using diffusion models, potentially offering a continuous, real-time alternative to traditional fluorescence videos without contrast agents.

Another is the integration of AI-powered imaging techniques like MA-DenseUNet with augmented reality (AR) or virtual reality (VR), overlaying real-time vascular information directly onto the surgical field. This could provide surgeons an intuitive, hands-free interface for critical data access, advancing AI-enhanced surgical environments.

Finally, our cross-modality framework offers potential for non-invasive diagnostics beyond OR. Synthetic MTT imaging could facilitate microvascular health assessments or chronic condition monitoring, such as peripheral artery disease (PAD), in outpatient settings. This label-free, detailed vascular assessment provides adaptability across diagnostic applications.

## VI. CONCLUSION

This study highlights the transformative potential of deep learning-driven cross-modality generation in advancing intraoperative imaging. By generating synthetic MTT images from label-free modalities, the MA-DenseUNet model—enhanced by statistical gating to address depth mismatches between modalities—offers a robust solution for real-time vascular assessment, accompanied by dramatically reducing imaging time and eliminating the need for ICG contrast agents. Its capacity to provide precise, real-time insights into blood flow and vessel structure could revolutionize surgical procedures, enhancing speed, safety, and efficiency.

As AI technology progresses, methods like the one proposed here are poised to become integral in modern surgical practices. By tackling current challenges and uncovering new pathways for innovation, this approach has potential to expand possibilities in both intraoperative imaging and non-invasive diagnostics.

## REFERENCES

- [1] V. L. Fredrickson, J. J. Russin, B. A. Strickland, J. Bakhsheshian, and A. P. Amar, "Intraoperative imaging for vascular lesions," *Neurosurgery Clinics*, vol. 28, no. 4, pp. 603-613, 2017.
- [2] C. Nimsky and B. Carl, "Historical, current, and future intraoperative imaging modalities," *Neurosurgery Clinics*, vol. 28, no. 4, pp. 453-464, 2017.
- [3] O. Goren, S. J. Monteith, M. Hadani, M. Bakon, and S. Harnof, "Modern intraoperative imaging modalities for the vascular neurosurgeon treating intracerebral hemorrhage," *Neurosurgical Focus*, vol. 34, no. 5, p. E2, 2013.
- [4] M. Yamamoto, S. Sasaguri, and T. Sato, "Assessing intraoperative blood flow in cardiovascular surgery," *Surgery today*, vol. 41, pp. 1467-1474, 2011.
- [5] M. Sekijima *et al.*, "An intraoperative fluorescent imaging system in organ transplantation," in *Transplantation proceedings*, 2004, vol. 36, no. 7: Elsevier, pp. 2188-2190.
- [6] M. Kusano, N. Kokudo, M. Toi, and M. Kaibori, "ICG fluorescence imaging and navigation surgery," Springer, 2016.
- [7] M. G. Lubner, L. Mankowski Gettle, D. H. Kim, T. J. Ziemlewicz, N. Dahiya, and P. Pickhardt, "Diagnostic and procedural intraoperative ultrasound: technique, tips and tricks for optimizing results," *The British journal of radiology*, vol. 94, no. 1121, p. 20201406, 2021.
- [8] K. Bekelis, S. Missios, A. Desai, C. Eskey, and K. Erkmén, "Magnetic resonance imaging/magnetic resonance angiography fusion technique for intraoperative navigation during microsurgical resection of cerebral arteriovenous malformations," *Neurosurgical Focus*, vol. 32, no. 5, p. E7, 2012.
- [9] A. Scerrati *et al.*, "Indocyanine green video-angiography in neurosurgery: A glance beyond vascular applications," *Clinical Neurology and Neurosurgery*, vol. 124, pp. 106-113, 2014 2014, doi: 10.1016/j.clineuro.2014.06.032.
- [10] M. V. Marshall *et al.*, "Near-infrared fluorescence imaging in humans with indocyanine green: a review and update," *Open surgical oncology journal (Online)*, vol. 2, no. 2, p. 12, 2010 2010.
- [11] Y. Kumon, H. Watanabe, S. Ohue, and T. Ohnishi, "ICG videoangiography in neurosurgical procedures," *ICG Fluorescence Imaging and Navigation Surgery*, pp. 31-45, 2016 2016.
- [12] T. Ku and C. Choi, "Noninvasive optical measurement of cerebral blood flow in mice using molecular dynamics analysis of indocyanine green," *PLoS One*, vol. 7, no. 10, p. e48383, 2012 2012.
- [13] S. M, S. T, H. H, N. S, W. H, and K. K, "Quantitative Blood Flow Assessment by Multiparameter Analysis of Indocyanine Green Video Angiography," *World neurosurgery*, vol. 116, pp. e187-e193, 2021 2021, doi: 10.1016/j.wneu.2018.04.148.
- [14] M. Hope-Ross *et al.*, "Adverse reactions due to indocyanine green," *Ophthalmology*, vol. 101, no. 3, pp. 529-533, 1994 1994.
- [15] J. Oda *et al.*, "Intraoperative near-infrared indocyanine green--videoangiography (ICG--VA) and graphic analysis of fluorescence intensity in cerebral aneurysm surgery," *Journal of Clinical Neuroscience*, vol. 18, no. 8, pp. 1097-1100, 2011 2011.
- [16] S. Morales-Conde, E. Licardie, I. Alarcón, and A. Balla, "Indocyanine green (ICG) fluorescence guide for the use and indications in general surgery: recommendations based on the descriptive review of the literature and the analysis of experience," *Cirugía Española (English Edition)*, vol. 100, no. 9, pp. 534-554, 2022 2022.

- [17] H. Akbari and Y. Kosugi, "Hyperspectral imaging: A new modality in surgery," in *Recent advances in biomedical engineering*: IntechOpen, 2009.
- [18] K. Kuznetsov, R. Lambert, and J. F. Rey, "Narrow-band imaging: potential and limitations," *Endoscopy*, vol. 38, no. 01, pp. 76-81, 2006 2006.
- [19] W. Heeman, W. Steenbergen, G. M. van Dam, and E. C. Boerma, "Clinical applications of laser speckle contrast imaging: a review," *Journal of biomedical optics*, vol. 24, no. 8, pp. 080901-080901, 2019 2019.
- [20] J. Yu, G. Xu, P. Miao, and S. Tong, "Label-free Intraoperative Blood Flow Imaging and Augmented Reality Display in Surgical Microscope," in *2021 10th International IEEE/EMBS Conference on Neural Engineering (NER)*, 2021: IEEE, pp. 222-225.
- [21] Y. LeCun, Y. Bengio, and G. Hinton, "Deep learning," *nature*, vol. 521, no. 7553, pp. 436-444, 2015.
- [22] D. Briers *et al.*, "Laser speckle contrast imaging: theoretical and practical limitations," *Journal of biomedical optics*, vol. 18, no. 6, pp. 066018-066018, 2013 2013.
- [23] J. Goldberg *et al.*, "Intraoperative laser speckle contrast imaging to assess vessel flow in neurosurgery: a pilot study," *Neurosurgery*, vol. 94, no. 5, pp. 983-992, 2024 2024.
- [24] Z. Li, F. Liu, W. Yang, S. Peng, and J. Zhou, "A survey of convolutional neural networks: analysis, applications, and prospects," *IEEE transactions on neural networks and learning systems*, vol. 33, no. 12, pp. 6999-7019, 2021.
- [25] V. V. Tuchin, "Tissue optics and photonics: light-tissue interaction," *Journal of Biomedical Photonics & Engineering*, vol. 1, no. 2, pp. 98-134, 2015 2015.
- [26] Z. Feng *et al.*, "Perfecting and extending the near-infrared imaging window," *Light: Science & Applications*, vol. 10, no. 1, p. 197, 2021 2021.
- [27] P. Miao, Y. Zhang, C. Wang, and S. Tong, "Random matrix description of dynamically backscattered coherent waves propagating in a wide-field-illuminated random medium," *Applied Physics Letters*, vol. 120, no. 4, 2022 2022.
- [28] Y. Zhang, C. Wang, S. Tong, and P. Miao, "Separating single-and multiple-scattering components in laser speckle contrast imaging of tissue blood flow," *Biomedical Optics Express*, vol. 13, no. 5, pp. 2881-2895, 2022 2022.
- [29] Y. Guo *et al.*, "Random matrix-based laser speckle contrast imaging enables quasi-3D blood flow imaging in laparoscopic surgery," *Biomedical Optics Express*, vol. 14, no. 4, pp. 1480-1493, 2023 2023.
- [30] D. Qiao *et al.*, "Spectral domain isolation of ballistic component in visible light OCT based on random matrix description," *APL Photonics*, vol. 8, no. 4, 2023 2023.
- [31] G. Huang, Z. Liu, L. Van Der Maaten, and K. Q. Weinberger, "Densely connected convolutional networks," in *Proceedings of the IEEE conference on computer vision and pattern recognition*, 2017, pp. 4700-4708.
- [32] S. Woo, J. Park, J.-Y. Lee, and I. S. Kweon, "Cbam: Convolutional block attention module," in *Proceedings of the European conference on computer vision (ECCV)*, 2018, pp. 3-19.
- [33] M. Jang, H. Ruan, I. M. Vellekoop, B. Judkewitz, E. Chung, and C. Yang, "Relation between speckle decorrelation and optical phase conjugation (OPC)-based turbidity suppression through dynamic scattering media: a study on in vivo mouse skin," *Biomedical optics express*, vol. 6, no. 1, pp. 72-85, 2014 2014.
- [34] D. D. Postnov, J. Tang, S. E. Erdener, K. Kılıç, and D. A. Boas, "Dynamic light scattering imaging," *Science advances*, vol. 6, no. 45, p. eabc4628, 2020 2020.
- [35] J. W. Goodman, *Speckle phenomena in optics: theory and applications*. Greenwood Village, CO, United States: Roberts and Company Publishers, 2007.
- [36] S. R. Buló, L. Porzi, and P. Kotschieder, "In-place activated batchnorm for memory-optimized training of dnns," in *Proceedings of the IEEE conference on computer vision and pattern recognition*, 2018, pp. 5639-5647.
- [37] C.-Y. Lee, S. Xie, P. Gallagher, Z. Zhang, and Z. Tu, "Deeply-supervised nets," in *Artificial intelligence and statistics*, 2015: Pmlr, pp. 562-570.
- [38] L. G. Brown, "A survey of image registration techniques," *ACM computing surveys (CSUR)*, vol. 24, no. 4, pp. 325-376, 1992 1992.
- [39] U. Sara, M. Akter, and M. S. Uddin, "Image quality assessment through FSIM, SSIM, MSE and PSNR—a comparative study," *Journal of Computer and Communications*, vol. 7, no. 3, pp. 8-18, 2019 2019.
- [40] L. Wang, S. L. Jacques, and L. Zheng, "MCML—Monte Carlo modeling of light transport in multi-layered tissues," *Computer methods and programs in biomedicine*, vol. 47, no. 2, pp. 131-146, 1995 1995.
- [41] S. C. Feng, F. Zeng, and B. Chance, "Monte Carlo simulations of photon migration path distributions in multiple scattering media," in *Photon Migration and Imaging in Random Media and Tissues*, 1993, vol. 1888: SPIE, pp. 78-89.
- [42] F. Bevilacqua, D. Pignet, P. Marquet, J. D. Gross, B. J. Tromberg, and C. Depeursinge, "In vivo local determination of tissue optical properties: applications to human brain," *Applied optics*, vol. 38, no. 22, pp. 4939-4950, 1999 1999.
- [43] H. Wang, C. Magnain, S. Sakadžić, B. Fischl, and D. A. Boas, "Characterizing the optical properties of human brain tissue with high numerical aperture optical coherence tomography," *Biomedical optics express*, vol. 8, no. 12, pp. 5617-5636, 2017 2017.
- [44] Y. Murai, S. Nakagawa, F. Matano, K. Shirokane, A. Teramoto, and A. Morita, "The feasibility of detecting cerebral blood flow direction using the indocyanine green video angiography," *Neurosurgical review*, vol. 39, pp. 685-690, 2016 2016.
- [45] S. F. Chen *et al.*, "The application of intraoperative near-infrared indocyanine green videoangiography and analysis of fluorescence intensity in cerebrovascular surgery," *Surgical Neurology International*, vol. 2, 2011 2011.